

PUBLISHED VERSION

Josef A. Giddings, Yvonne M. Stokes, Kyle J. Bachus, and Heike Ebendorff-Heidepriem
Wet chemical etching of single-bore microstructured silicon dioxide fibers
Physics of Fluids, 2020; 32(7):073314-1-073314-13

© 2020 Author(s). Published under license by AIP Publishing

This article may be downloaded for personal use only. Any other use requires prior permission of the author and AIP Publishing. This article appeared in *Physics of Fluids*, 2020; **32(7):073314-1-073314-13** and may be found at <http://dx.doi.org/10.1063/5.0014335>

PERMISSIONS

<https://publishing.aip.org/resources/researchers/rights-and-permissions/sharing-content-online/>

For institutional or funder-designated repositories (e.g., DOE Pages)

- You may deposit the accepted manuscript immediately after acceptance, using the credit line formatting below
- You may **deposit the VOR 12 months after publication**, with the credit line and a link to the VOR on AIP Publishing's site

Format for credit lines

- After publication please use: "This article may be downloaded for personal use only. Any other use requires prior permission of the author and AIP Publishing. This article appeared in (citation of published article) and may be found at (URL/link for published article abstract).
- Prior to publication please use: "The following article has been submitted to/accepted by [Name of Journal]. After it is published, it will be found at [Link](#)."
- For Creative Commons licensed material, please use: "Copyright (year) Author(s). This article is distributed under a Creative Commons Attribution (CC BY) License."

25 February 2022

<http://hdl.handle.net/2440/127539>


Wet chemical etching of single-bore microstructured silicon dioxide fibers

Cite as: Phys. Fluids **32**, 073314 (2020); <https://doi.org/10.1063/5.0014335>

Submitted: 19 May 2020 • Accepted: 06 July 2020 • Published Online: 24 July 2020

 Josef A. Giddings,  Yvonne M. Stokes,  Kyle J. Bachus, et al.

COLLECTIONS

 This paper was selected as Featured



View Online



Export Citation



CrossMark

ARTICLES YOU MAY BE INTERESTED IN

[Effects of gravity and surface tension on steady microbubble propagation in asymmetric bifurcating airways](#)

Physics of Fluids **32**, 072105 (2020); <https://doi.org/10.1063/5.0012796>

[Flow-induced fractionation effects on slip of polydisperse polymer melts](#)

Physics of Fluids **32**, 073109 (2020); <https://doi.org/10.1063/5.0017996>

[Numerical study on immersed granular collapse in viscous regime by particle-scale simulation](#)

Physics of Fluids **32**, 073313 (2020); <https://doi.org/10.1063/5.0015110>



Author Services

English Language Editing

High-quality assistance from subject specialists

LEARN MORE







Wet chemical etching of single-bore microstructured silicon dioxide fibers

Cite as: Phys. Fluids 32, 073314 (2020); doi: 10.1063/5.0014335

Submitted: 19 May 2020 • Accepted: 6 July 2020 •

Published Online: 24 July 2020



Josef A. Giddings,^{1,a)}  Yvonne M. Stokes,¹  Kyle J. Bachus,^{2,3}  and Heike Ebendorff-Heidepriem² 

AFFILIATIONS

¹Department of Applied Mathematics, University of Adelaide, South Australia 5005, Australia

²Institute for Photonics and Advanced Sensing, School of Physical Sciences, University of Adelaide, South Australia 5005, Australia

³Trajan Scientific and Medical, Ringwood, Australia

^{a)} Author to whom correspondence should be addressed: josef.giddings@outlook.com

ABSTRACT

We model the process of wet chemical etching of the external surface of a single-bore microstructured silicon dioxide fiber in hydrofluoric acid (HFA) while water is pumped through the internal channel to prevent etching of it. The model uses the Stokes flow for the velocity throughout the system and the advection–diffusion equation for the concentration of HFA. We determine the etch rate as a function of HFA concentration using data from experiments designed for this purpose, from which we calculate the change in the fiber surface. We solve our equations using a time-stepping finite-element method and verify our model by comparing to results found experimentally. We investigate the effects of different water flow rates, diffusivity, buoyancy, and bore radius. We find the water being pumped through the bore does not fully protect it and there is some etching of the internal channel, which is difficult to see in experimental images. We also obtain an estimate of the diffusivity of high-concentration HFA in water.

Published under license by AIP Publishing. <https://doi.org/10.1063/5.0014335>

I. INTRODUCTION

Microstructured silicon dioxide (SiO₂) fibers are glass fibers of 100 μm–200 μm diameter with one or more internal channels of 2 μm–10 μm diameter running along their length. Aside from their use as optical fibers and sensors, such fibers are used in the fabrication of axicon microlenses, whereby a cone-shaped tip is formed at one end using fiber polishing,^{1,2} focused ion beam technology,^{3,4} or etching with hydrofluoric acid (HFA).^{5–7} Recently, microstructured SiO₂ fibers have been used to produce emitter tips for electrospray ionization mass spectrometry. The sensitivity of electrospray ionization mass spectrometry is enhanced by reducing the size of droplets leaving the emitter tip, with the droplet size being influenced by both channel diameter and the distance beyond the channel wet by the fluid because of surface tension. Thus, improving performance is heavily dependent on emitter tip geometry and the flow rate of the biomolecule solution being analyzed. Based on industry requirements, this paper is focused on the development of emitter tips that can operate at nano-flow rates, each of which is an axisymmetric cylinder with a single channel (the bore) of constant diameter having

a tip that tapers to a very small outer diameter, a little larger than the bore diameter, at the tip end. The taper should be sufficiently long and/or of a shape to minimize wetting around the bore. To make such an emitter tip, a fiber is first drawn with a constant bore diameter of 2 μm–10 μm and outer diameter of 125 μm. A method is then needed to produce the tapered tip at one end.

One method is to heat a portion of the fiber and pull the ends to stretch the heated region; breaking or cleaving at the narrowest point yields two finely tapered needle-like tips. However, this typically results in emitter tips with a tapered bore, which are susceptible to clogging. To maintain a uniform bore diameter along the emitter tip while forming an external taper, a new fabrication process is being developed, whereby the end of a fiber is dipped in HFA while pumping water through the internal channel,⁵ as depicted in Fig. 1. The intention is to etch away the outer surface of the fiber while maintaining a constant bore diameter. The water entering the HFA solution from the fiber bore both protects the internal channel from etching and creates a concentration gradient around the fiber end, which determines the geometry etched. Experiments have shown that higher flow rates create wider, convex geometries, while

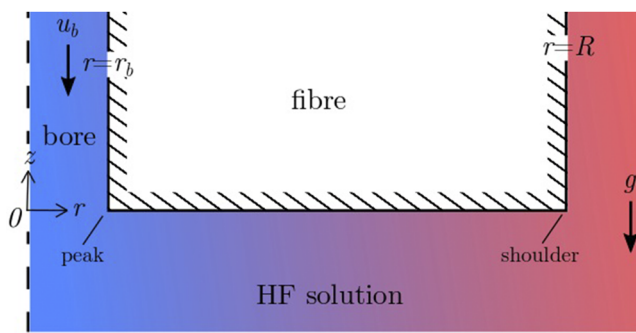
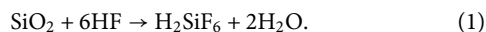


FIG. 1. A longitudinal section through an axisymmetric fiber dipped in hydrofluoric acid (HFA), showing the initial geometry in the (r, z) plane, where r is the radial coordinate and z is the axial coordinate. Water is pumped through the bore of the fiber into the HFA solution.

lower flow rates create narrower, concave geometries more suitable for emitter tips.

In this paper, we describe a mathematical model of the etching process and its numerical solution. Numerical results are compared with experiments to validate the model, and the model is used to investigate the influence of the key parameters, including the flow rate of the water and the etching time, on the final geometry of the emitter tip. As will be seen, the model results have highlighted outcomes of the etching process not previously identified by experiment, in particular, some etching of the internal channel despite the flow of protecting water through it. Furthermore, the model has brought to light improvements in the experimental setup needed for repeatable production of emitter tips.

Hydrofluoric acid is a solution of hydrogen fluoride (HF) in water, which is commonly used to etch and polish glass due to its high reactivity with SiO_2 molecules. The generally accepted chemical reaction governing the etching of SiO_2 by HF is^{8,9}



In concentrations of HF above 48% by weight, the HF spontaneously forms noxious fumes, so decreasing the liquid concentration unpredictably. As a result, it is common practice in the etching of SiO_2 to use HFA with 48% HF by weight in order to maximize the etching properties of the HFA, while maintaining predictable etch rates and safety.

Noulty and Least¹⁰ investigated the diffusivity of HFA in water experimentally for HFA solutions of 0.002%–0.2% HF by weight, with measurements at stronger concentrations being unsuccessful due to the formation of bubbles of HF vapor. They found a slight variation in HFA diffusivity at these low HF concentrations. However, due to a lack of data, the dependence of the diffusivity on concentration at higher HFA concentrations is not known and we shall assume a constant diffusivity as is common in the modeling of etching using HFA.^{11,12}

Our model for the etching of an axisymmetric single-bore microstructured fiber is described in Sec. II. We use the advection–diffusion equation, with advection driven by the change in fluid density with HFA concentration, to model HFA transport and concentration. Because of the low Reynolds number of the flow, we

assume the Stokes flow. We use (1) to calculate the flux of HFA at the fiber surface due to etching. Section III describes our method for numerical solution of our model, for which we use the finite-element software package *FEniCS*. In Sec. IV, we investigate how the various model parameters influence the geometry of the etched tip and, in Sec. V, compare model predictions with experimental results. Conclusions and avenues for future investigation are given in Sec. VI.

We here note that the injection of a lower density fluid below the surface of a higher density fluid, as in our problem, drives a free-convection flow (see Sec. III), which has some features in common with buoyant plumes. In particular at the bore outlet where the lower density water is forced into the higher density acid, a structure forms akin to the vortex ring associated with starting forced plumes as studied by Gao and Yu,¹³ although it is not carried much below the outlet because of the low Reynolds number of the flow. Furthermore, the entrainment flow that develops is similar to that driven by a buoyant plume as, for example, seen in Vajipeyajula *et al.*¹⁴ Nevertheless, the changing fiber geometry due to etching affects the flow and, in turn, the concentration profile, making our problem more complex.

While the problem of interest in this paper is the etching of SiO_2 fibers with hydrofluoric acid while water is pumped through the bore, the model is applicable to the etching of many materials, including natural quartz, fused silica, doped silica, borosilicate, sodium silicate and conductive glass, bulk metallic glasses and stainless steel, using many etchants such as hydrofluoric acid, ammonium bifluoride, nitric acid, sulfuric acid, hydrochloric acid, or hydrogen peroxide, and a non-reactive liquid other than water may be pumped through the bore. Therefore, for generality, our model is derived for a concentration-dependent diffusivity of the reactive fluid in the non-reactive fluid. In order to use the model for other etching problems, suitable relations must be determined and used for the (possibly concentration-dependent) diffusivity, the concentration-dependent density of the etchant, the concentration-dependent etch rate, and the flux of etchant at the material surface due to etching. This will have a quantitative, but likely not qualitative, effect on the results contained in this paper.

II. THE MATHEMATICAL MODEL

As shown in Fig. 1, we model the system in axisymmetric cylindrical coordinates $\mathbf{r} = (r, z)$, with the z axis directed vertically upward along the central axis of the fiber. At initial time ($t = 0$), the bottom of the fiber is at $z = 0$. The r axis measures distance radially outward from the central axis, and gravity is directed downward such that $\mathbf{g} = (0, -g)$. Initially, the fiber has bore radius r_b and outer radius R . Because of the similarity in the viscosities of water and HFA, we assume a constant fluid viscosity μ throughout the entire system. For convenience, we refer to the intersection of the fiber bottom with the internal bore wall as the “peak” and the intersection of the fiber bottom with the external wall as the “shoulder.”

A. Velocity

We model the flow profile, $\mathbf{u} = (u_r, u_z)$, as Stokes flow with the Boussinesq approximation for buoyancy due to the density

difference between water and HFA. The density of HFA is greater than that of water, and we assume the fluid density to be

$$\rho = \rho(c) = \rho_a - B(c), \quad (2)$$

where c is the volume fraction of 48% HF by weight HFA, which has density ρ_a , and $B(c) \geq 0$ with $B(1) = 0$. This gives us the mass and momentum conservation equations as

$$\nabla \cdot \mathbf{u} = 0, \quad (3)$$

$$\nabla p = \mu \nabla^2 \mathbf{u} - \mathbf{g}B(c), \quad (4)$$

where p is pressure and ∇ is the del operator in axisymmetric cylindrical coordinates. For concentrations of HF in water up to 48% by weight, the density of HFA is close to linear in c , so that the density is given by (2) with

$$B(c) = (1 - c)(\rho_a - \rho_w), \quad (5)$$

where ρ_w is the density of pure water.

The volume flux of water through the bore is denoted Q . We place an inlet boundary across the bore at $z = 20r_b$, which is sufficiently far from $z = 0$ that the HFA concentration is zero and no etching of the bore occurs in its vicinity. The flow through this inlet is modeled as Poiseuille flow in the negative z direction; that is, the flow velocity at the inlet boundary is $\mathbf{u} = (0, -u_b)$, where

$$u_b = \frac{2Q}{\pi r_b^4} (r_b^2 - r^2) \quad \text{for } 0 \leq r \leq r_b. \quad (6)$$

On the surface of the fiber, we have no slip $\mathbf{u} = \mathbf{0}$. We place outer boundaries at $r = 50r_b$ and $z = \pm 50r_b$, which are far from the bore outlet but within the HFA solution surrounding the fiber, on which we apply the no stress conditions

$$[p\mathbf{I} + \mu(\nabla\mathbf{u} + (\nabla\mathbf{u})^T)] \cdot \mathbf{n} = \mathbf{0}, \quad (7)$$

where \mathbf{I} is the identity matrix and $\mathbf{n} = (n_r, n_z)$ is the unit outward normal vector to the boundary, i.e., directed outward from the fluid.

B. Concentration

We model the concentration of HFA using the advection-diffusion model, given in axisymmetric cylindrical coordinates by

$$\frac{\partial c}{\partial t} = \nabla \cdot (D(c)\nabla c) - \mathbf{u} \cdot \nabla c, \quad (8)$$

where $D(c)$ is the concentration-dependant diffusivity and $c = 1$ is water containing 48% by weight HF, i.e., the strongest possible HFA concentration.

As indicated by (1), there is a loss of HF at the fiber surface due to etching, which we include in the model as a flux condition on the fiber boundary. Let $ER(c)$ be the thickness of SiO_2 removed per unit time due to etching, which we refer to as the etch rate. From (1), we calculate the molar flux of HF due to etching, j_e , as six times the number of moles of SiO_2 etched per unit time, that is,

$$j_e = 6 \frac{\rho_S ER}{M_S}, \quad (9)$$

where the density and molar mass of SiO_2 are ρ_S and M_S , respectively. Multiplying (9) by the molar mass of HF, M_{HF} , we convert from the molar flux to the mass flux of HF molecules. Noting that the mass concentration of HF molecules is given by $0.48\rho_a c$, we have, using Fick's law,

$$-0.48\rho_a D(c) \frac{\partial c}{\partial \mathbf{n}} = 6 \frac{M_{HF}}{M_S} \rho_S ER$$

or

$$-D(c) \frac{\partial c}{\partial \mathbf{n}} = 12.5 \frac{M_{HF}}{M_S} \frac{\rho_S}{\rho_a} ER \quad (10)$$

at the fiber boundary. The loss of HF mass due to etching is accompanied by a small gain of H_2SiF_6 and H_2O , which we have neglected in our model.

At the inlet boundary, we have pure water, $c = 0$, at the outer boundaries $r = 50r_b$ and $z = 50r_b$, we assume no diffusive flux, $D(c)\partial c/\partial \mathbf{n} = 0$, and at the lower boundary $z = -50r_b$, we assume we are sufficiently far from the fiber that the fluid is pure HFA, $c = 1$. Water is pumped through the fiber until it has reached a steady state before the fiber is placed in the HFA; hence, we have the initial condition

$$c = \begin{cases} 0 & \text{if } r \leq r_b \text{ and } z \geq 0, \\ 1 & \text{otherwise.} \end{cases} \quad (11)$$

C. Etch rate and moving fiber surface boundary

We denote the location of the fiber surface at time t in parametric form as $\mathbf{r}_f = (r_f(t), z_f(t))$. The equation governing the fiber surface location is given by

$$\frac{d}{dt}(\mathbf{r}_f) = ER \mathbf{n}. \quad (12)$$

For the etch rate function $ER(c)$, we use the relation given by Monk *et al.*,¹²

$$ER = k_1 c^\alpha (1 + k_2 c^\beta), \quad (13)$$

where k_1, k_2, α , and β are positive constants. It has been shown (see, for example, Spierings⁹) that the relationship between concentration and etch rate is close to linear at low concentrations c when $ER \approx k_1 c^\alpha$ and, hence, we expect $\alpha \approx 1$.

To determine appropriate parameter values for (13), we performed experiments, whereby silica fibers were held in solutions of different HFA concentration, c , for different amounts of time and the thickness etched found from the difference in the fiber diameters before and after. We then computed the experimental etch rate ER for each c and, finally, the parameter values (see Table I) that gave a best fit between (13) and our data. Further details are given in Appendix A.

D. Non-dimensionalization

With reference to the typical dimensional parameters for our problem, as given in Table I, we now introduce scaled variables, denoted by tildes and defined by

$$\mathbf{r} = r_b \tilde{\mathbf{r}}, \quad \mathbf{u} = k_1 k_2 \tilde{\mathbf{u}}, \quad t = \frac{r_b}{k_1 k_2} \tilde{t}, \quad p = \frac{\mu k_1 k_2}{r_b} \tilde{p}. \quad (14)$$

TABLE I. Values of the parameters and variables used.

Parameter	Value	Units
ρ_a	1.15×10^3	kg/m ³
ρ_w	1.00×10^3	kg/m ³
ρ_S	2.65×10^3	kg/m ³
M_{HF}	20.01×10^{-3}	kg/mol
M_S	60.08×10^{-3}	kg/mol
μ	9×10^{-4}	Pa s
r_b	$2 \times 10^{-6} - 5 \times 10^{-6}$	m
R	62.5×10^{-6}	m
k_1	7.639×10^{-9}	m/s
k_2	2.475	
α	1	
β	2.296	
Q	$1 \times 10^{-14} - 3 \times 10^{-12}$	m ³ /s
D	$1 \times 10^{-9} - 2 \times 10^{-8}$	m ² /s

We also define the dimensionless parameters

$$\mathbf{B}_c = -\mathbf{g} \frac{r_b^2(\rho_a - \rho_w)}{\mu k_1 k_2}, \quad U_c = \frac{2Q}{\pi k_1 k_2 r_b^2}, \quad J_c = 12.5 \frac{M_{HF} \rho_S}{M_S \rho_a}, \quad (15)$$

and the dimensionless diffusivity function

$$\tilde{D}(c) = \frac{D(c)}{r_b k_1 k_2}. \quad (16)$$

Our dimensional model is then, dropping the tildes for convenience,

$$\nabla \cdot \mathbf{u} = 0, \quad (17)$$

$$\nabla p = \nabla^2 \mathbf{u} + \mathbf{B}_c(1 - c), \quad (18)$$

$$\frac{\partial c}{\partial t} = \nabla \cdot (D(c) \nabla c) - \mathbf{u} \cdot \nabla c, \quad (19)$$

subject to the initial condition

$$c = \begin{cases} 0 & \text{if } r \leq 1 \text{ and } z \geq 0, \\ 1 & \text{otherwise} \end{cases} \quad (20)$$

and boundary conditions as follows: On the inlet boundary $z = 20$, $0 \leq r \leq 1$, we have

$$\mathbf{u} = (0, -u_b), \quad (21)$$

$$c = 0, \quad (22)$$

where $u_b = U_c(1 - r^2)$. On the surface of the fiber, \mathbf{r}_f ,

$$\mathbf{u} = \mathbf{0}, \quad (23)$$

$$D(c) \frac{\partial c}{\partial \mathbf{n}} = -J_c \left[c^\alpha \left(\frac{1}{k_2} + c^\beta \right) \right], \quad (24)$$

$$\frac{d}{dt}(\mathbf{r}_f) = c^\alpha \left(\frac{1}{k_2} + c^\beta \right) \mathbf{n}. \quad (25)$$

On the outer boundaries $r = 50$ and $z = 50$,

$$[-p\mathbf{I} + (\nabla \mathbf{u} + (\nabla \mathbf{u})^T)] \cdot \mathbf{n} = \mathbf{0}, \quad (26)$$

$$D(c) \frac{\partial c}{\partial \mathbf{n}} = 0. \quad (27)$$

On the outer boundary $z = -50$,

$$[-p\mathbf{I} + (\nabla \mathbf{u} + (\nabla \mathbf{u})^T)] \cdot \mathbf{n} = \mathbf{0}, \quad (28)$$

$$c = 1. \quad (29)$$

III. NUMERICAL SIMULATION

We solve our model using a time-stepping finite-element method within the software package *FEniCS*. Let Δt be the time step size and $t_n = n\Delta t$ denote the time at the n th time step. Using the first-order implicit Euler method to approximate (19) and (25) where we have linearized (19), we obtain

$$c^{n+1} = c^n + \Delta t \{ \nabla \cdot (D(c^n) \nabla c^{n+1}) - \mathbf{u}^n \cdot \nabla c^{n+1} \}, \quad (30)$$

$$\mathbf{r}_f^{n+1} = \mathbf{r}_f^n + \Delta t \left\{ (c^{n+1})^\alpha \left(\frac{1}{k_2} + (c^{n+1})^\beta \right) \mathbf{n} \right\}. \quad (31)$$

We also use the automatic mesh generation facility in *FEniCS* to generate an unstructured triangular mesh over the spatial flow domain having nodes $i = 1, \dots, I$ with coordinates (r_i, z_i) .

Now, given the computational domain and concentration $c^n(r_i, z_i)$ at time t_n , we

1. solve (17) and (18), using $c^n(r_i, z_i)$ and subject to (21), (23), (26), and (28), for the flow velocity $\mathbf{u}^n(r_i, z_i)$ and pressure $p^n(r_i, z_i)$ at time t_n ;
2. solve (30), subject to (22), (24), (27), and (29), to determine $c^{n+1}(r_i, z_i)$ at the next time t_{n+1} ;
3. solve (31) at each boundary node of the fiber to determine its new location and so update the fiber boundary;
4. redistribute nodes on boundaries and, using the inbuilt automatic re-meshing class in *FEniCS*, adjust the mesh over the domain;
5. interpolate the solution $c^{n+1}(r_i, z_i)$ onto the new mesh.

We then increment n and repeat this procedure. Beginning with $n = 0$ and our initial conditions, we thus obtain the solution at discrete times t_n , $n = 0, 1, \dots$

The updating of the fiber boundaries and redistribution of mesh nodes warrant further discussion. In general, the normal \mathbf{n} used in (31) to update the coordinates of a node on the fiber boundary is the average of the normals of the two neighboring boundary segments. However, to compute new positions of a peak or shoulder point (defined in Sec. II and shown in Fig. 1), we compute new end points of each of the neighboring boundary segments using the normal to that segment and then take the new peak or shoulder point to be the intersection of the two new boundary segments so obtained. This is illustrated in Fig. 2 for the shoulder node, where the crosses mark the boundary node positions and the solid lines joining them show the boundary segments at the given time, the circles mark

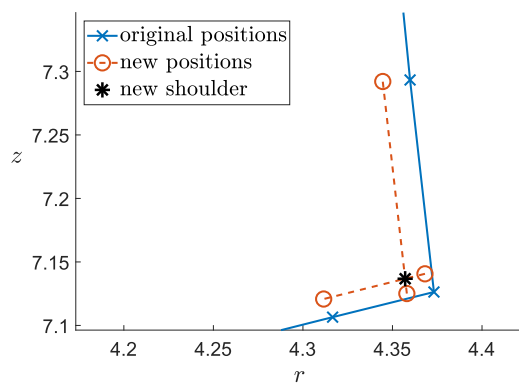


FIG. 2. An example of the placement of the shoulder node.

the new end points and the dashed lines show the new positions of the boundary segments computed in the manner just described, and the asterisk marks the new position of the shoulder node at the intersection of the new boundary segments. To avoid a mesh and

computational problems (due to the decrease over time of the distance between a peak/shoulder node and its neighboring boundary nodes, or the possible complete removal of a boundary segment), we then redistribute the nodes on the fiber surface each side of the peak/shoulder so as to maintain their original separation ratios.

We also redistribute the nodes on all other boundaries in order to avoid excessive mesh distortion. Finally, we use *FEniCS* inbuilt automatic re-meshing class to redistribute the internal nodes. Figure 3 shows examples of the mesh at $t = 0$ and $t = 5$. Although we can see there is some compression of the mesh elements around the peak and some stretching of the elements around the shoulder, these effects are significantly reduced due to our mesh updating method described above.

Results from a typical simulation for a fiber with external and bore radii of $62.5 \mu\text{m}$ and $5 \mu\text{m}$, respectively, corresponding to dimensionless external and bore radii of 12.5 and 1, respectively, are shown in Fig. 4. A flux of $Q = 50 \text{ nl/min} = 8.333 \text{ m}^3/\text{s}$ and diffusion coefficient of $D = 10^{-8} \text{ m}^2/\text{s}$ have been assumed with all other physical parameters as given in Table 1, yielding dimensionless parameters $\mathbf{B}_c = -2161.952 \mathbf{k}$, $U_c = 1.122 \times 10^6$, $\tilde{D} = 1.058 \times 10^5$, and $J_c = 9.593$. Shown are the fiber geometry and fluid velocity at the given times, together with the updated HFA concentration computed from these.

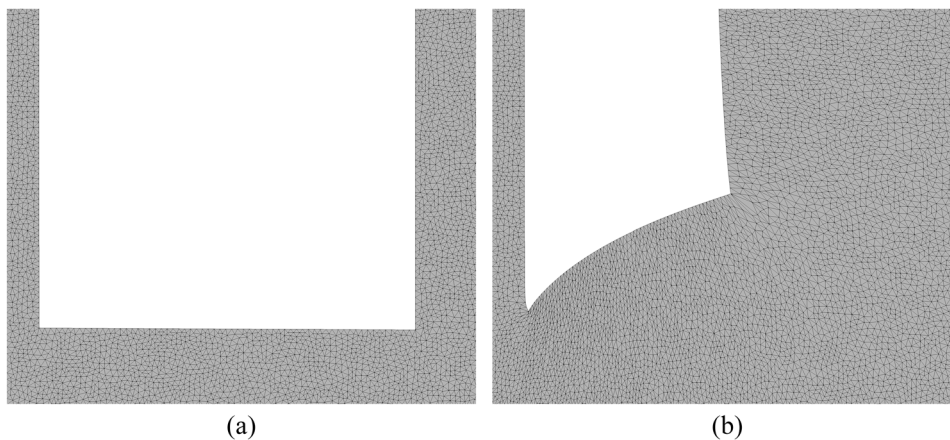


FIG. 3. A computational mesh at (a) $t = 0$ and (b) $t = 5$ showing the distortion of the mesh due to the movement of the fiber boundary.

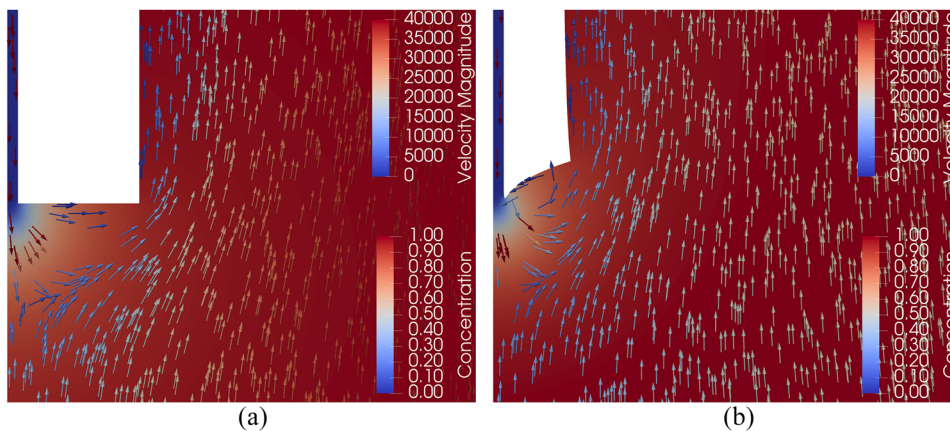


FIG. 4. Fiber geometry, together with the velocity (vectors) and concentration (shading) of the surrounding HFA, at times (a) $t = \Delta t = 0.01$ and (b) $t = 5$ for a fiber with external and bore radii of $62.5 \mu\text{m}$ and $5 \mu\text{m}$, and with a flux $Q = 50 \text{ nl/min} = 8.333 \text{ m}^3/\text{s}$ and diffusivity $D = 10^{-8} \text{ m}^2/\text{s}$.

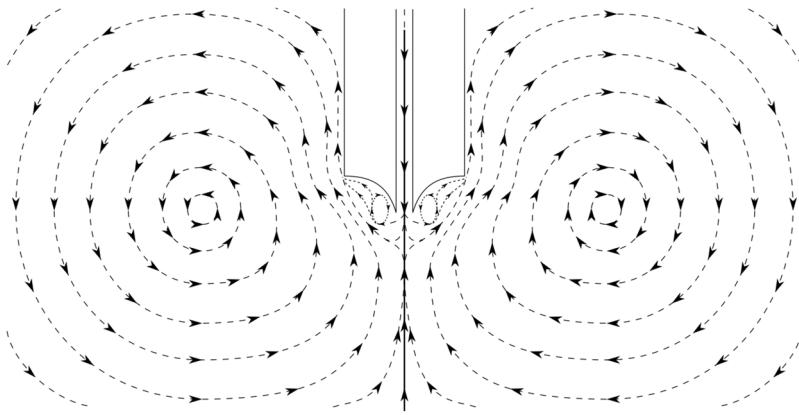


FIG. 5. A schematic of the flow profile on formation of a sharp peak.

The color of the background is scaled with c and its color bar is shown in the bottom right of the figure. The arrows show the direction of the flow and are colored with the magnitude of \mathbf{u} for $0 \leq |\mathbf{u}| \leq 4 \times 10^4$ and with no color variation for $4 \times 10^4 \leq |\mathbf{u}| \leq U_c$, the corresponding color bar being at the top right.

We see that the HFA concentration near the peak is low and increases with distance from the peak to the maximum, $c = 1$ (48% HF by weight). The decrease in fluid density with decreasing HFA concentration drives a flow circulation (not seen in the portion of the computational domain shown in Fig. 4). Buoyancy drives the flow upward in the regions of lower HFA concentration near the fiber, while far away the flow is downward. Focusing on the velocity near the peak, we see that the velocity of the water coming out of the bore is quickly slowed and we find the water flux through the bore mainly affects the velocity profile through the dilution of the HFA. As the fiber etches and a sharper peak forms, as in Fig. 4(b), we find a vortex forms just to the side of the peak, which leads to a higher etch rate in this area by slowing dilution of the HFA. A schematic of this flow profile is shown in Fig. 5.

IV. PARAMETER INVESTIGATION

In order to improve our understanding of the etching process, we now examine how the bore radius r_b and flux Q through the bore affect the solution. In addition, because at the high HFA concentrations used in etching the diffusivity D and its sensitivity to HFA concentration are unknown, we assume a constant diffusivity and consider the effect of its value on the solution. Table I gives the range of values for each of D , r_b , and Q over which we investigate. All other model parameters are considered to be fixed with values as given in Table I. Because of the applicability of the model to etching with other reactive and non-reactive fluids, we conclude this section with a brief investigation of the effect of changing the density difference between the non-reactive and reactive fluids.

The water entering the HFA from the fiber bore creates a water “blanket” around the bore outlet (recall that HFA is more dense than water) into which HFA diffuses. The greater the flux Q , the greater the extent of the “blanket” around the bore outlet, and the greater the distance the HFA must travel through this “blanket” in order to

etch the fiber. The protection provided by this water “blanket” will depend on the magnitude of the diffusivity; the larger the diffusivity, the less effective the water “blanket.” It is to be expected that the etching of the fiber over time will depend on the balance between the advective flux of water and the diffusive flux of HFA, i.e., the ratio

$$F = \frac{U_c}{D} = \frac{2Q}{\pi r_b D}. \quad (32)$$

Figure 6 shows the effects of varying F on the geometry of a fiber with initial bore radius $5 \mu\text{m}$, which, for a fiber of external radius $R = 62.5 \mu\text{m}$, corresponds to a dimensionless external radius $R/r_b = 12.5$; the solid lines correspond to fixed $D = 10^{-8} \text{ m}^2/\text{s}$ and varying $Q = \pi r_b D F / 2$, and the dashed lines correspond to fixed $Q = 50 \text{ nl/min}$ and varying $D = 2Q / (\pi r_b F)$. From this figure, we can see greater etching for smaller F and a similar fiber profile for different choices of Q and D corresponding to the same value F . A large F means a weak HFA concentration adjacent to the fiber, which increases slowly from the peak to the shoulder of the fiber so that etching takes longer and results in a convex shape on the bottom of the fiber, at least in the short term. Conversely, small F means a large HFA concentration adjacent to the fiber, a faster increase from the peak to the shoulder, more rapid etching, and a concave shape on the fiber bottom due to etching. Note that the increasing HFA concentration along the initially vertical outer surface of the fiber from the shoulder to the surface of the HFA solution into which the fiber is dipped leads to more etching of this surface with distance from the shoulder, as shown in Fig. 6(b). Finally, it is apparent from Fig. 6(b) that a small value F results, after a sufficiently long time, in a fiber of small diameter at which point there is little change in HFA concentration from peak to shoulder and a fairly uniform etch rate across the bottom of the fiber.

For convenience, we now define $(r_{pk}(t), z_{pk}(t))$ and $(r_{sr}(t), z_{sr}(t))$ to be the (dimensionless) coordinates of the peak and shoulder at time t , where $(r_{pk}(0), z_{pk}(0)) = (1, 0)$ and $(r_{sr}(0), z_{sr}(0)) = (12.5, 0)$. As shown in Fig. 6, for all values of F , there is, initially, more vertical etching at the shoulder than at the peak so that the tip amplitude, defined to be the vertical distance $z_{sr}(t) - z_{pk}(t)$ between the peak and the shoulder, initially increases over time. For sufficiently small F , the rapid increase in HFA concentration with radial

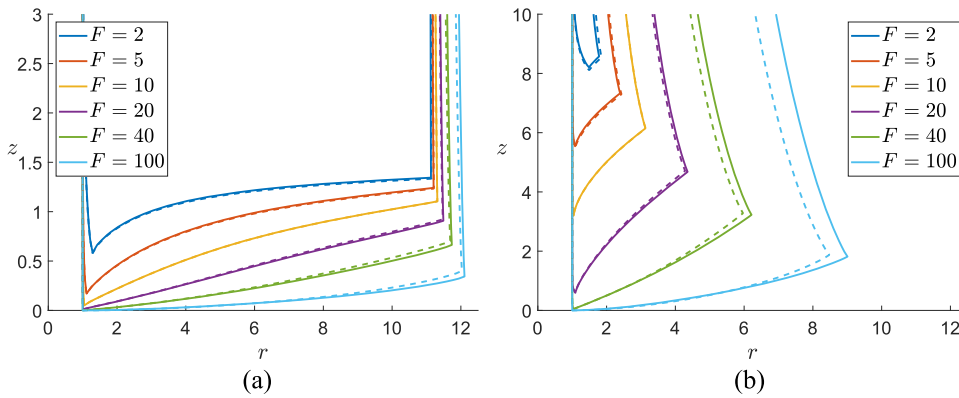


FIG. 6. Fiber geometry at times (a) $t = 1$ and (b) $t = 8$ for different values F . Solid lines: fixed $D = 10^{-8} \text{ m}^2/\text{s}$, varying $Q = \pi r_b D F / 2$. Dashed lines: fixed $Q = 50 \text{ nl/min}$, varying $D = 2Q / (\pi r_b F)$. Here, the initial dimensionless external fiber radius is $R/r_b = 12.5$. (Note, r and z are scaled with r_b .)

distance from the peak results in the fiber bottom becoming more steep in the neighborhood of the peak and the tip becoming quite pointed/sharp in this region. Eventually, further etching of the inner bore wall and externally in this region results in the removal of the sharp tip such that the vertical coordinate z_{pk} of the peak increases, as demonstrated in Fig. 7. In addition, after sufficient time, the overall narrowing of the fiber reduces the radial distance $r_{sr} - r_{pk}$ between the shoulder and the peak and the change in HFA concentration from peak to shoulder decreases. Together, these two effects result at later time in greater etching at the peak compared with the shoulder and a reduction in the tip amplitude over time. This initial increase and subsequent decrease in the tip amplitude over time are shown, for various values of F , in Fig. 8. For this and subsequent figures, the diffusivity was held constant at $D = 10^{-8} \text{ m}^2/\text{s}$ with the value of F varied by changing the water flux Q through the bore; as in Fig. 6, the initial dimensionless external radius of the fiber was $R/r_b = 12.5$. Very similar curves are obtained if the water flux is held fixed and the diffusivity is varied.

Because the bore is not fully protected by the flow, there is some increase in the peak radius, and the bore in the neighborhood of the peak, due to etching. For larger values of F , this increase is very

small; however, as F decreases, it becomes more significant due to the increase in HFA concentration at the peak; see, for example, Fig. 6, $F = 2$, noting that $r = 1$ is the initial dimensionless bore radius. However, if the peak region then becomes pointed/sharp and further etching removes the very tip as described above, then the peak radius may subsequently reduce. Figure 9(a) shows the radial coordinate r_{pk} of the peak against time for different values of F , while Fig. 9(b) shows r_{pk} vs F at different times. We see that for large F , the peak radius increases progressively with time over the duration of the simulation. However, for smaller F , the peak radius first increases and then decreases with time. The values of F that give rise to the steepest HFA concentration gradients on the tip ($F \sim 10$), i.e., those that produce the most tapered tip shape from peak to shoulder, give the greatest reduction of the peak radius after the initial increase. We note from Fig. 9(b) that the change in peak radius at $t = 8$ is similar for $F \sim 40$ and $F \sim 10$, while Fig. 6(b) shows that $F \sim 10$ gives the tip with the sharper, narrower taper.

For very low values of F , it is possible for the peak and shoulder to join. An example is shown in Fig. 10 for $F = 1$, where we see significantly more etching of the bore and increase in the peak radius compared to the examples examined earlier, due to a higher HFA

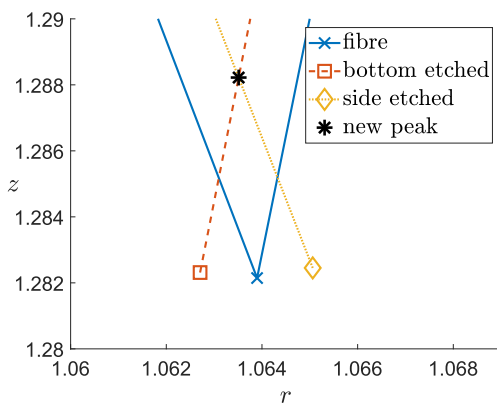


FIG. 7. Etching at the peak when the fiber bottom becomes steep in its neighborhood and further etching results in the removal of the tip end.

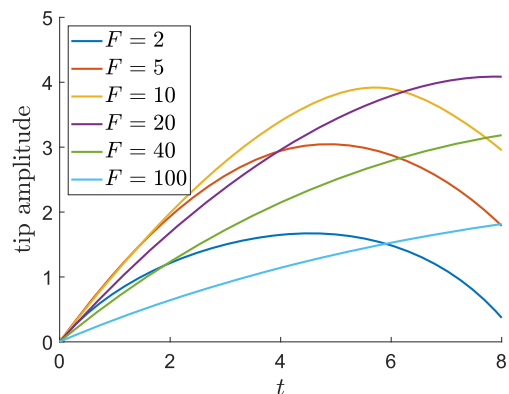


FIG. 8. Tip amplitude $z_{sr} - z_{pk}$ vs time t for a range of values F ; $R/r_b = 12.5$.

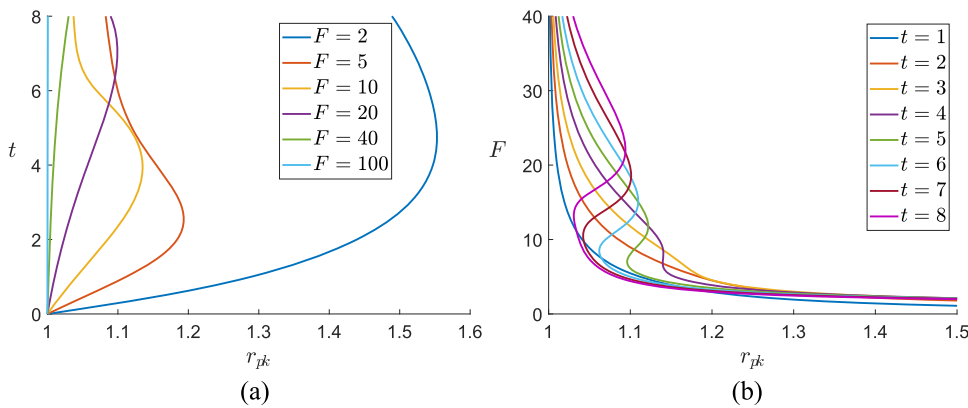


FIG. 9. Dependence of the radial coordinate r_{pk} vs (a) time t at the given values of F , and (b) F at the given times t ; $R/r_b = 12.5$.

concentration at the peak. In this example, there is a relatively small gradient in the HFA concentration from peak to shoulder and therefore a small tip amplitude and blunt end to the fiber. There is also no decrease in the peak radius at later time. Eventually, the peak and shoulder positions meet, which causes our numerical method to fail due to the loss of a boundary segment. However, beyond this, we would expect further etching of the external fiber wall to reduce the peak/shoulder radius and, so, lead to a very slender and fragile fiber whose bore radius increases smoothly from $r = 1$ to $r = r_{pk}$ at the outlet.

We next consider the effect of decreasing the initial bore radius, i.e., increasing the initial dimensionless fiber radius R/r_b , while holding the diffusivity D and flux Q constant. As seen from the definition of F , see (32), this parameter increases with decreasing r_b . Moreover, changing r_b by a factor p corresponds to changing the initial fiber radius in the dimensionless problem by the factor $1/p$ and, in addition, changes the time scale by a factor p , see (14). Thus, the effect of changing r_b is not that of a simple change in F and, therefore, we compare the physical geometry over physical time for different bore radii r_b . Decreasing r_b results in a faster flow through the bore, greater penetration into the HFA, a lower HFA concentration at the peak, and slower etching in the neighborhood of the peak.

However, the effect is local with very small change in the geometry at the shoulder. This is seen in Fig. 11, which shows the shape of the fiber tip after 30 min of etching with water flux Q nl/min through the bore for $r_b = 2.5 \mu\text{m}$ and $r_b = 5 \mu\text{m}$; for both values r_b , the initial external radius is $R = 62.5 \mu\text{m}$ and the diffusivity is held fixed at $D = 10^{-8} \text{m}^2/\text{s}$. In particular, there is little change in the etched fiber width.

We conclude this section with an investigation of how the difference in density between the reactive etchant (HFA) and non-reactive fluid (water), i.e., the buoyancy of the non-reactive fluid relative to the denser reactive fluid, affects the outcome. To do this, we simply replace \mathbf{B}_c with $k_b \mathbf{B}_c$ for a constant $k_b \geq 0$, see (15). The smaller the value of k_b , the smaller the density difference. Note that $k_b < 1$ corresponds to reactive and non-reactive fluids with a density difference smaller than that of 48% HFA and water, which might result from a weaker HFA solution. On the other hand, since 48% HFA is the strongest practical HFA solution, $k_b > 1$ corresponds to a completely different etchant and/or a non-reactive fluid other than water. We find that $k_b > 1$ results in more etching in a given amount of time compared with $k = 1$, while $k < 1$ results in less etching. However, the change is very small, as shown in Fig. 12. The

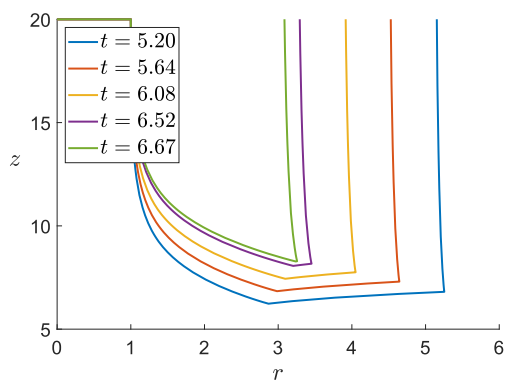


FIG. 10. Etching over time t of a fiber with initial external radius $R/r_b = 12.5$ and $F = 1$, showing the joining of the peak and shoulder at $t = 6.67$.

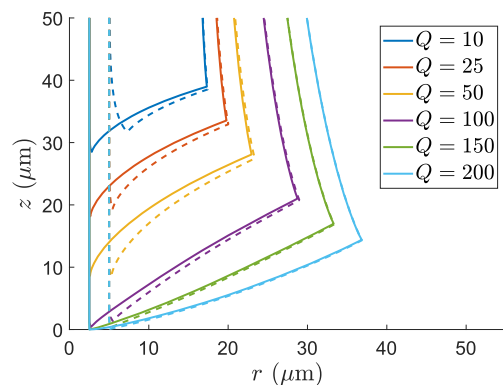


FIG. 11. Fiber profiles for $r_b = 2.5 \mu\text{m}$ (solid) and $5 \mu\text{m}$ (dashed) after 30 min of etching with flux Q nl/min through the bore. In each case, $R = 62.5 \mu\text{m}$ and $D = 10^{-8} \text{m}^2/\text{s}$.

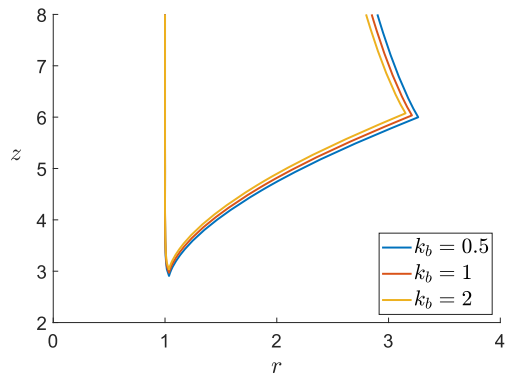


FIG. 12. Effect of the density difference between reactive and non-reactive fluids expressed as $k_b(\rho_a - \rho_w)$, for $F = 10$ at time $t = 8$.

flow in the etchant is quite weak and, while driven by the buoyancy of the non-reactive fluid entering the HFA through the fiber bore, is not very sensitive to its magnitude, with halving or doubling the density difference having very little effect on the outcome, provided the magnitude is sufficiently large to dominate the inertia of the flux through the bore.

Our investigation into the parameters of our system has shown that the etching of the fiber is not sensitive to the bore radius (within a practical range) or the buoyancy of the non-reactive fluid relative to the etchant. The system is, however, sensitive to the ratio of the advective flux Q and the diffusive flux (measured by D), through the effect on the magnitude of the parameter F . This parameter determines the HFA concentration profile, which, in turn, has a profound impact on the final etched profile. Higher diffusivity or lower advective flux creates a stronger concentration gradient along the fiber bottom and sharp peaks, while low diffusivity or high advective flux results in a smaller HFA concentration gradient and less sharp peaks. Hence, in order to control the geometry of the fiber tip, the flux Q and diffusivity D must be such that a HFA concentration profile with both the required strength and gradient is obtained.

V. COMPARISON WITH EXPERIMENTS

In addition to the modeling described above, an experimental investigation of etching has been carried out and we here compare model and experimental results. Fibers of nominal external radius $R = 62.5 \mu\text{m}$ and bore radius $r_b = 5 \mu\text{m}$ were dipped into 48% by weight hydrofluoric acid to a depth of 2 cm, with each fiber in its own test tube such that its axis was aligned with the central axis of the test tube and perpendicular to the HFA surface. A fiber was left to etch for a period T of 10 min, 15 min, 25 min, 30 min, or 32.5 min during which time water was pumped through the fiber bore with a flow rate Q of 25 nl/min, 50 nl/min, or 100 nl/min. On account of the low pressure required at low flow rates, 25 nl/min was found to be the minimum flow rate possible at which the pump in use could provide a consistent flow. After the allotted time T , each fiber was removed from the acid and dipped into a test tube of water in order to wash any remaining acid off the fiber surface. The experiment for each combination of time T and flow rate Q was completed in triplicate to demonstrate consistency.

After etching, a picture of each fiber was taken under an optical microscope and imported into the image processing and analysis package *ImageJ*, which was used to obtain the external shape of the fiber as a set of (X, Y) coordinates in pixels. These data were then manipulated to obtain the geometry as a set of (x, z) coordinates in μm , with the center of the bore outlet at the origin and the fiber axis on the vertical z axis. Note that the carets are used on the vertical coordinate because the origin in this coordinate system is shifted vertically compared with the coordinate system of the model. **Figure 13(a)** shows the profile of the etched tip of a fiber, so obtained. Strictly, in this figure, the points through the fiber bore are not in the cross-sectional plane of those on the sides. Hence, we neglected the data points within the fiber bore and kept only those corresponding to the sides of the fiber tip. Then, bearing in mind that data from an ideal experiment would be axisymmetric, we split the data into two sets of points $(r, z) = (|x|, z)$, one for each side of the fiber tip. Finally, we determined the degree six polynomial of best fit for each of the two sets of data. **Figure 13(b)** shows the modified data and polynomials corresponding to **Fig. 13(a)**, where the blue and red points correspond to the left and right sides of the fiber tip, respectively, and the solid and dashed lines are the polynomials of best fit

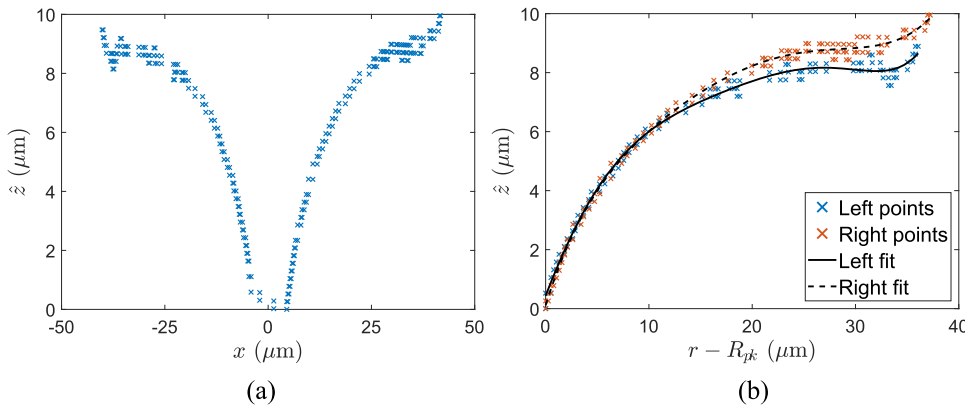


FIG. 13. (a) Fiber tip profile as shown by plotting (x, z) data points from *ImageJ* and (b) data points $(r = |x|, z)$ showing the asymmetry in the fiber tip profile, where we have subtracted the final dimensional peak radius R_{pk} from r ; $Q = 25 \text{ nl/min}$, $T = 15 \text{ min}$, $R \approx 62.5 \mu\text{m}$, $r_b \approx 5 \mu\text{m}$.

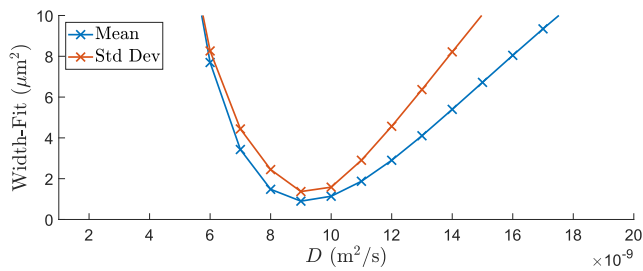


FIG. 14. Mean (blue) and standard deviation (red) of the Width-Fit vs diffusivity D .

for the left and right sides of the fiber tip, respectively. The asymmetry clearly evident in the profile is most likely caused by the fiber axis not being exactly perpendicular to the acid surface during etching, so that, with the bottom of the fiber being at an angle to the horizontal, the buoyant water would flow more readily in the direction of greatest slope resulting in a more dilute HFA concentration profile and less etching in this direction.

As already mentioned, the experiment for each combination of etch time T and flow Q was repeated three times. For each (T, Q) pair, we computed average measurements of the geometry as follows: For each fiber, measurements were taken of the initial

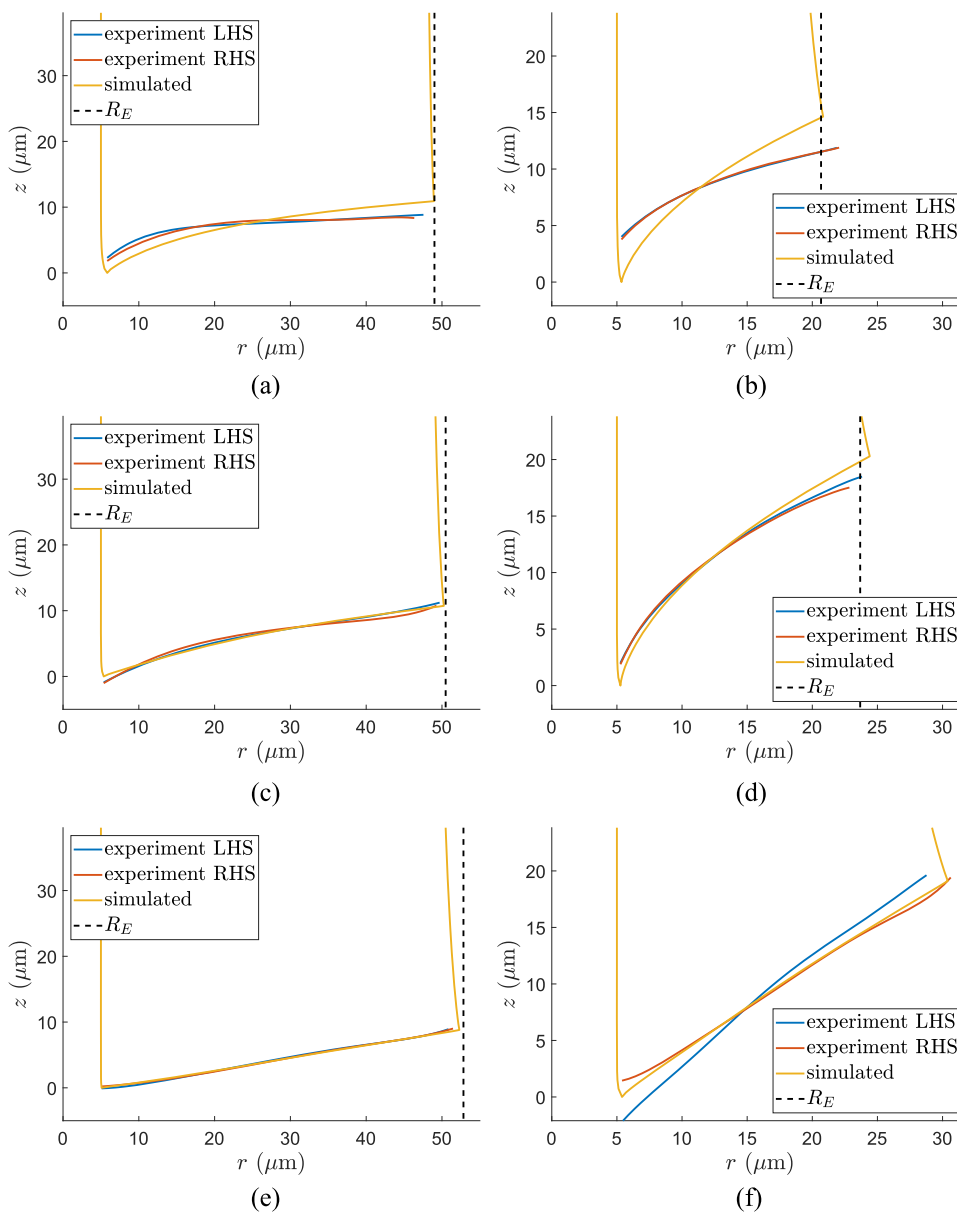


FIG. 15. Simulated and experimental fiber tip profiles after etching for (a) $Q = 25$ nl/min, $T = 10$ min; (b) $Q = 25$ nl/min, $T = 30$ min; (c) $Q = 50$ nl/min, $T = 10$ min; (d) $Q = 50$ nl/min, $T = 30$ min; (e) $Q = 100$ nl/min, $T = 10$ min; (f) $Q = 100$ nl/min, $T = 30$ min. $D = 9 \times 10^{-9}$ m²/s was assumed for the simulations. The experimental LHS and RHS curves are the best-fit polynomials of degree 6 to the experimental data. Also shown is the experimentally determined shoulder radius R_E .

external radius R and the shoulder radius after etching, R_{sr} , from which the radial change at the shoulder, $R - R_{sr}$, was determined. Although there was some small variation in R and R_{sr} across the three repetitions for given (T, Q) , there was relatively less variation in $R - R_{sr}$. Now, before etching, the mean fiber radius across all fibers (with radii ranging from $60 \mu\text{m}$ to $65 \mu\text{m}$) was $\bar{R} = 63.235 \mu\text{m}$ and we defined the experimental shoulder radius after etching for given (T, Q) to be

$$R_E = \bar{R} - (\overline{R - R_{sr}}), \quad (33)$$

where $\overline{R - R_{sr}}$ is the average radial change at the shoulder over the three repetitions.

To compare these data with our model, we ran simulations for a fiber with initial external radius $R = 63.235 \mu\text{m}$ and bore radius $r_b = 5 \mu\text{m}$. Because the diffusivity of HFA in water is not known, we ran simulations for each (T, Q) pair with values of $D = (1, 2, 3 \dots, 20) \times 10^{-9} \text{ m}^2/\text{s}$ and, for each triple (T, Q, D) , obtained the physical shoulder radius $R_{sr} = r_b r_{sr}$ and the shape of the tip as the set of (r, z) coordinates at the grid points on the tip surface from the peak to the shoulder. Since in emitter operation, wetting around the bore may extend to the shoulder radius and affect the size of droplets leaving the emitter, this is an important dimension on which we focused to determine the diffusivity D that gives the best fit of our model with the experimental data. Thus, from the simulation data, we computed the “Width-Fit” for each (T, Q, D) , defined as

$$\text{Width-Fit} = (R_E - R_{sr})^2, \quad (34)$$

where R_E is the experimental shoulder radius defined above. Then, for each value $D = \mathcal{D}$, we computed the mean and standard deviation of the Width-Fit across all triples (T, Q, \mathcal{D}) . As shown in Fig. 14, both the mean and standard deviation of the Width-Fit are smallest for $D = 9 \times 10^{-9} \text{ m}^2/\text{s}$, from which we conclude that $D = 9 \times 10^{-9} \text{ m}^2/\text{s}$ is a good estimate of the diffusivity of HFA in water.

Figure 15 shows the geometry of the emitter tip as given by the simulation, and the experimental shoulder radius R_E , for different etching periods T and flows Q . There is good agreement between R_E and the shoulder radius from the simulation in each case. In addition, overlaying the tip profiles from the simulation for each (T, Q) are the polynomials that were fitted to the experimental data for one of the three repetitions. Note that, because of the method for determining R_E , its value does not necessarily correspond to the shoulder radius for any individual repetition. There is excellent agreement between experiment and simulation for the larger flows $Q = 50 \text{ nl/min}$ and 100 nl/min , allowing that the difference in the polynomials for $(T, Q) = (30 \text{ min}, 100 \text{ nl/min})$ indicates asymmetry in the experimental setup. There is, however, less agreement between experiment and simulation for the low flow $Q = 25 \text{ nl/min}$. This is expected to be largely due to the flow being at the lower bound of the range over which the pump is reliable, especially given that significantly more fluctuation in the pressure reading was observed than for the higher flow rates.

We note also that it was not possible to accurately measure the bore radii of the fibers used for the experiments. However, it is likely that, as with the external fiber radius, there was variation in the bore radius around the nominal value of $r_b = 5 \mu\text{m}$. As we have seen in Sec. IV, although the shoulder radius is not strongly dependent on the bore radius, changing the bore radius does affect the tip

geometry, especially in the neighborhood of the peak and at low flow rate; see Fig. 11. Thus, variation in the bore radius might be a cause of some of the discrepancy between simulation and experiment at lower flow rates.

In light of the potential and known variation in the initial geometry of the fibers, the evident lack of axisymmetry in the experimental setup, and the lack of reliability of the pump at low flow rate, we conclude that our model, with constant diffusivity $D = 9 \times 10^{-9} \text{ m}^2/\text{s}$, is a good predictor of etching.

VI. CONCLUSION

We have developed the first model for the process of wet chemical etching of axisymmetric single-bore microstructured silicon dioxide fibers in hydrofluoric acid (HFA) while water is pumped through the bore. Through numerical simulation, we found that the advective flux of water through the bore and the diffusivity of HFA in water significantly affect the system, with these parameters determining the concentration profile of the acid on the fiber boundary. We found the key quantity to be the balance between advective flux and diffusive flux, namely the dimensionless parameter

$$F = \frac{2Q}{\pi r_b D},$$

where Q is the volumetric flow rate of water through the channel, D is the diffusivity of HFA in water, and r_b is the bore radius. Since D is a property of the reactive and non-reactive fluids, and with specified r_b , Q is the key parameter for control of the tip geometry and therefore of the performance of an emitter tip for electrospray ionization mass spectrometry made in this manner.

We have also shown that the flow of water through the bore does not fully protect it from etching, which may increase the radius of the bore around the outlet and indeed completely remove part of the tip. This had not been previously detected in experiments and was revealed by the modeling.

We found that small F results in a narrow, concave tip but with an increase in the bore radius around the outlet due to etching. Large F reduces the etching around the bore outlet but yields wider convex tips. A larger bore outlet suggests larger droplet size; a wider convex-shaped tip suggests more wetting and larger droplet size also. Since small droplet size is needed to improve the efficiency of electrospray ionization mass spectrometry, our simulations indicate there is an optimal value of F , which yields the smallest droplet size. Then, it appears possible to select the flow rate Q , which gives the best shaped tip; reducing the bore radius may also help. Work is needed to determine how shape affects wetting in order to determine the optimal initial fiber geometry and flow rate Q .

By comparing simulations with experiments, we have shown our model to be a good predictor of etching for a constant diffusivity of high-concentration HFA in water of $D \approx 9 \times 10^{-9} \text{ m}^2/\text{s}$. To our knowledge, this is the first estimate for the diffusivity of HFA with around 48% HF by weight. It compares with the value $D \approx 2 \times 10^{-9} \text{ m}^2/\text{s}$ found by Noulty and Leait¹⁰ for HFA with no more than 0.2% HF by weight. Other work is needed to confirm our result. With more precise knowledge of this diffusivity, the initial fiber geometry, and pump flow rates, it is expected that the accuracy of our model output would improve.

A natural continuation of this work would be to consider multi-bore microstructured fibers, which are of interest as emitter tips. Although this would require a three-dimensional model, the model developed in this paper is applicable and symmetry of the channel pattern might be exploited to reduce the domain to a three-dimensional wedge.

ACKNOWLEDGMENTS

This work was supported by the Australian Research Council through Linkage Project (Grant No. LP160100657) to Y.M.S., H.E.-H., and industry partner Trajan Scientific and Medical, along with a Future Fellowship (Grant No. FT160100108) to Y.M.S. This work was performed in part at the OptoFab Node of the Australian National Fabrication Facility (ANFF), a company established under the National Collaborative Research Infrastructure Strategy to provide nano- and microfabrication facilities for Australia's researchers, utilizing Commonwealth and South Australia State Government funding. The authors wish to thank Dr. Brendan Harding for his help and support with the development of the numerical code using the *FEniCS* software package.

APPENDIX: ETCH RATE AS A FUNCTION OF HFA CONCENTRATION

A summary of reaction-rate expressions applicable to chemical etching is given by Monk *et al.*¹² To determine which of these expressions to use and appropriate parameter values, we performed experiments, whereby silica fibers were held in solutions of different HFA concentration for different amounts of time and the thickness etched found from the difference in the fiber diameters before and after. The experiment for each combination of HFA concentration and hold time was performed in triplicate and the average etch thickness computed. Dividing this thickness by the time taken gave the etch rate.

The experiments were run using fibers $\sim 330 \mu\text{m}$ in diameter. Solutions of different concentration were made by diluting 48% by weight HFA ($c = 1$) with water; HFA volume fractions of 25%, 50%, 75%, and 100% were used yielding solutions with $c = 0.25, 0.5, 0.75,$ and 1 , respectively. Hold times of 5 min, 10 min, 15 min, and 30 min were used. Table II shows the average etch rate for each combination of HFA concentration and hold time. Also shown is the overall average of the etch rates for a given HFA concentration. These values fit well with values in the literature.⁹ Measurements of fiber diameter and, hence, of computed etch thickness have a tolerance of $\pm 1.5 \mu\text{m}$. As a result, the etch rates for the lower concentrations are less reliable than those for the higher concentrations.

TABLE II. Average etch rates in nm/s for different etch times and HF concentrations.

c	5 min	10 min	15 min	30 min	Average
0.25	2.618	2.545	2.278	1.576	2.254
0.5	5.090	6.617	5.575	5.017	5.575
0.75	15.125	11.562	12.944	12.944	13.144
1	27.923	25.960	26.275	25.960	26.529

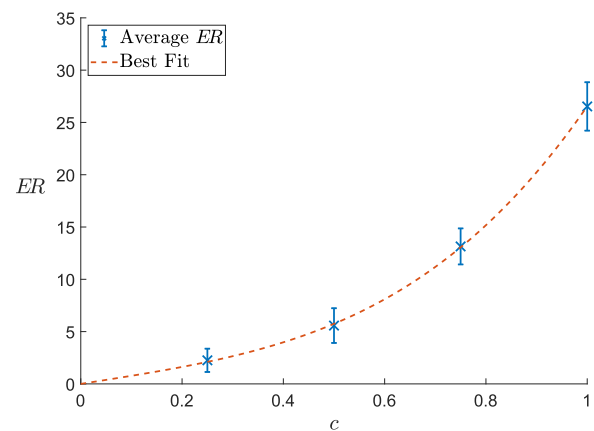


FIG. 16. Etch rate ER (nm/s) vs concentration c . Red dashed curve: as given by (13) with parameters (A1). Blue crosses and tolerance bars: as computed from experimental data.

To determine which etch rate relation gives the best fit to our experimental data, we first used a least squares algorithm to determine the relevant parameters for each etch rate relation. The relation given in (13) gave the smallest norm of the residuals, however gave a value of $\alpha < 1$ such that the etch rate had a very steep gradient at low HFA concentrations, which does not match experimental data. Hence, using the known linearity of the relationship between concentration and etch rate at low concentrations,⁹ we required $\alpha \geq 1$. On using the least squares algorithm for (13) with $\alpha \geq 1$ to obtain new parameters, we found that this relation still gave the lowest norm of the residuals. The best-fit parameters (4 sig. figs) were

$$k_1 = 7.639, \quad \alpha = 1.000, \quad k_2 = 2.475, \quad \beta = 2.296. \quad (\text{A1})$$

Figure 16 shows a plot of the average etch rates given in the final column of Table II, with tolerance bars showing one standard deviation, and the curve (13) with parameters (A1).

DATA AVAILABILITY

The data that support the findings of this study are available within the article.

REFERENCES

- ¹T. Grosjean, S. S. Saleh, M. A. Suarez, I. A. Ibrahim, V. Piquerey, D. Charrat, and P. Sandoz, "Fiber microaxicons fabricated by a polishing technique for the generation of Bessel-like beams," *Appl. Opt.* **46**(33), 8061–8067 (2007).
- ²E. U. Şimşek, B. Şimşek, and B. Ortaç, "CO₂ laser polishing of conical shaped optical fiber deflectors," *Appl. Phys. B* **123**(6), 176 (2017).
- ³S. Cabrini, C. Liberale, D. Cojoc, A. Carpentiero, M. Prasciolu, S. Mora, V. Degiorgio, F. De Angelis, and E. Di Fabrizio, "Axicon lens on optical fiber forming optical tweezers, made by focused ion beam milling," *Microelectron. Eng.* **83**(4–9), 804–807 (2006).
- ⁴H. Melkonyan, K. Sloyan, K. Twayana, P. Moreira, and M. S. Dahlem, "Efficient fiber-to-waveguide edge coupling using an optical fiber axicon lens fabricated by focused ion beam," *IEEE Photonics J.* **9**(4), 1–9 (2017).

- ⁵K. Bachus, E. S. d. L. Filho, K. Włodarczyk, R. Oleschuk, Y. Messaddeq, and H.-P. Loock, “Fabrication of axicon microlenses on capillaries and microstructured fibers by wet etching,” *Opt. Express* **24**(18), 20346–20358 (2016).
- ⁶S.-K. Eah, W. Jhe, and Y. Arakawa, “Nearly diffraction-limited focusing of a fiber axicon microlens,” *Rev. Sci. Instrum.* **74**(11), 4969–4971 (2003).
- ⁷A. Kuchmizhak, S. Gurbatov, A. Nepomniaschii, O. Vitrik, and Y. Kulchin, “High-quality fiber microaxicons fabricated by a modified chemical etching method for laser focusing and generation of Bessel-like beams,” *Appl. Opt.* **53**(5), 937–943 (2014).
- ⁸D. J. Monk, D. S. Soane, and R. T. Howe, “A review of the chemical reaction mechanism and kinetics for hydrofluoric acid etching of silicon dioxide for surface micromachining applications,” *Thin Solid Films* **232**(1), 1–12 (1993).
- ⁹G. A. C. M. Spierings, “Wet chemical etching of silicate glasses in hydrofluoric acid based solutions,” *J. Mater. Sci.* **28**(23), 6261–6273 (1993).
- ¹⁰R. A. Noulty and D. G. Leaist, “Diffusion of aqueous hydrofluoric acid and aqueous potassium fluoride,” *Electrochim. Acta* **30**(8), 1095–1099 (1985).
- ¹¹J. Liu, Y.-C. Tai, J. Lee, K.-C. Pong, Y. Zohar, and C.-M. Ho, “*In situ* monitoring and universal modelling of sacrificial PSG etching using hydrofluoric acid,” in *Proceedings IEEE Micro Electro Mechanical Systems* (IEEE, 1993), pp. 71–76.
- ¹²D. J. Monk, D. S. Soane, and R. T. Howe, “Hydrofluoric acid etching of silicon dioxide sacrificial layers II. Modeling,” *J. Electrochem. Soc.* **141**(1), 270–274 (1994).
- ¹³L. Gao and S. C. M. Yu, “Vortex ring formation in starting forced plumes with negative and positive buoyancy,” *Phys. Fluids* **28**(11), 113601 (2016).
- ¹⁴B. Vajipeyajula, T. Khambampati, and R. A. Handler, “Dynamics of a single buoyant plume in a FENE-P fluid,” *Phys. Fluids* **29**(9), 091701 (2017).